# Antimony Doped Tin Oxide–Synthesis, Characterization and Application as Cathode Material in Li-O₂ Cells: Implications on the Prospect of Carbon-Free Cathodes for Rechargeable Lithium-Air Batteries

**H. Beyer,[z] M. Metzger,* J. Sicklinger,* X. Wu, K. U. Schwenke, and H. A. Gasteiger\*\***

*Chair of Technical Electrochemistry, Department of Chemistry and Catalysis Research Center, Technical University of Munich, D-85748 Garching, Germany*

To develop reversible Li-O₂ batteries, the need for novel carbon-free cathode materials is evident. In this study, we present the hydrothermal synthesis of highly conductive crystalline antimony doped tin oxide (ATO) nanoparticles, the fabrication of ATO electrodes with high surface area, and their application as cathodes in aprotic Li-O₂ cells. We use a pressure transducer and an online electrochemical mass spectrometer to quantify consumed and evolved gases during discharge and charge of Li-O₂ cells. Solid discharge products on the cathode are identified by infrared spectroscopy and quantified by acid-base titration and UV-vis spectroscopy. Thus we demonstrate an unprecedented cell chemistry: In contrast to carbon cathodes, ATO cathodes enable the formation of Li₂O and prevent the formation of carbonates on the cathode surface. Formed Li₂O can be recharged at high potentials, which leads to the evolution of oxygen. These new mechanistic insights provide implications for cathode design concepts that might enable the reversible cycling of Li-O₂ cells.

Since its introduction in 1996,[1] the concept of an aprotic Li-air battery has attracted huge interest due to its outstanding theoretical energy density of ∼3400 Wh/kg on a material level.[2] The predicted energy density on a system level of 250–500 Wh/kg exceeds that of current Li-ion batteries by a factor of 1.5–2, but the practical advantages over advanced Li-ion battery technologies considered are as yet uncertain.[3] However, an improved understanding of Li-O₂ electrochemistry contributes to expanding the frontiers of electrochemistry and materials science.

The development of rechargeable Li-O₂ cells is facing major challenges such as low rate capability, low round trip efficiency and poor cycle life, as discussed in several review articles.[4–6] The cycle life of aprotic Li-O₂ cells with state of the art carbon cathodes fundamentally depends on the reversible formation/decomposition of lithium peroxide via the following 2 e⁻ cathode reaction:[7]

$$2Li^+ + 2e^- + O_2 \leftrightarrows Li_2O_2 \qquad \Delta E^\circ = 2.96\,V \qquad [1]$$
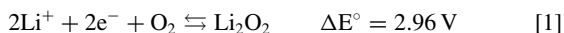
Further, the formation of Li₂O via a 4 e⁻ process, which would enable higher capacities, is theoretically possible:

$$4Li^+ + 4e^- + O_2 \leftrightarrows 2Li_2O \qquad \Delta E^\circ = 2.91\,V \qquad [2]$$
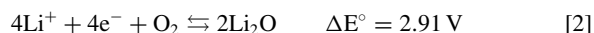
In the early stage of Li-O₂ battery research, Li₂O formation on carbon has indeed been claimed without experimental proof.[8,9] Li₂O has also been hypothesized to be a likely product using especially catalysts with a high M-O bond strength such as Pt.[10] However, experimental evidence for Li₂O formation has only been shown by Y.-C. Lu et al., notably on an oxide support: The authors detected minor amounts of Li₂O by in-situ ambient pressure X-ray photoelectron spectroscopy (APXPS) on LiₓV₂O₅ at a very low cell voltage.[11,12] Apart from this work, Li₂O has not been observed in Li-O₂ cells to date, and its formation on carbon materials has been explicitly excluded by differential electrochemical mass spectrometry (DEMS)[13] and XPS.[14] Moreover, Li₂O has been found to be non-rechargeable even at the decomposition potential of a diglyme electrolyte when using carbon electrodes artificially prefilled with Li₂O.[15]

The major hindrance of a reversible Li-O₂ cell chemistry are parasitic side reactions triggered by reactive intermediates of Reaction 1.

These have been identified as superoxide radicals formed during discharge,[16] and singlet oxygen (¹O₂) produced by the decomposition of Li₂O₂ during charge.[17] They are believed to cause the oxidation of both the carbon cathode and the electrolyte, with Li₂CO₃ as the prevailing product.[18] During charge, Li₂CO₃ is only partly removed from the electrode, thus accumulates during cycling and ultimately leads to capacity fading and cell failure.[19,20] The extent of carbon corrosion during discharge is still a matter of debate, whereas it is well documented during charge. Some authors reported the formation of a Li₂CO₃ layer on the cathode surface via chemical reaction of C with Li₂O₂ during discharge,[21,22] with additional Li₂CO₃ being formed by electrolyte degradation at the Li₂O₂/electrolyte interface.[21] Others reported carbon to be relatively stable during discharge, but found it to promote electrolyte decomposition to Li₂CO₃ and lithium carboxylates. In turn, they observed carbon degradation at charging potentials over 3.5 V.[23]

Therefore, the need for the development of carbon-free support materials is evident. Basic requirements are sufficient electronic conductivity to prevent the cathode from being the limiting component in charge transport, high surface area to allow reasonable capacities, chemical and electrochemical stability against Li₂O₂, O₂⁻• and ¹O₂, low cost and low environmental impact.

Outstanding cyclabilities of Li-O₂ cells with alternative cathode materials like nanoporous gold[24] and TiC[25] have been reported. However, the scientific community has not succeeded in reproducing these results to date, despite the strong interest and efforts that have arisen due to this work.[6] Furthermore, the performance of carbides and nitrides, which are potentially prone to oxidation, has been found to be strongly dependent on the formation of nanometric oxide surface films.[26,27] To circumvent these issues, electrically conductive metal oxides are promising materials due to their inherent stability against oxidation. Hence, the magnéli phase Ti₄O₇[28] as well as Pt supported on TiO₂ nanofibers[29] have been proposed as eligible compounds for Li-O₂ cathodes.

Among the conductive oxides, antimony-doped tin oxide (ATO) is probably the most extensively studied compound. The bulk and surface chemistry of SnO₂ is well-studied and has been the subject of a detailed review.[30] A variety of both surface-additives and lattice-dopants has been reported (Ref. [30] and sources therein), the most thoroughly studied lattice-dopant being antimony. Tin oxide based materials have been used for a wide range of applications from gas

sensing to Li ion battery anodes. The use of tin oxide based materials (among many other oxides) as Li ion battery anodes has recently been reviewed.[31] The working principle of $SnO_2$ anodes has been studied in detail.[32] It is based on lithium intercalation followed by an irreversible reduction of tin oxide to metallic tin under $Li_2O$ formation and further reversible lithiation by alloying to form $Li_xSn$. In the context of our present work, it is important to note that lithium intercalation does not commence at potentials above 1.5 V, tin oxide reduction and $Li_2O$ formation require potentials below 1 V and alloying only starts around 0.6 V.[33] Recently, the use of ruthenium-catalyzed ITO (indium-doped tin oxide)[34] and ruthenium-catalyzed ATO[35] as carbon-free cathodes for non-aqueous Li-$O_2$ batteries have been demonstrated. The latter study pointed out that the use of non-catalyzed ATO cathodes failed due to their insufficient electrical conductivity, whereas for Ru-ATO, good cyclability and outstanding capacity were shown. $Li_2O_2$ was identified as the only discharge product and was shown to form toroids at a discharge rate of 0.08 $\mu A/cm_{BET}^2$. Here it is interesting to note that at least for carbon based Li-air cathodes, the formation of toroids at low current densities in glyme-based electrolyte solutions has clearly been attributed to the presence of water/protons in the cell,[36,37] which has also been shown to result in dramatically increased discharge capacities.[38]

Our aim is to synthesize ATO nanoparticles, use them to fabricate non-catalyzed ATO electrodes with adequate electrical conductivity and high surface area, and apply them as cathodes in aprotic Li-$O_2$ cells. In this study, we present the hydrothermal synthesis of ATO nanoparticles from chloride-free precursors using a modified procedure first reported by Zhang and Gao,[39] followed by additional calcination and milling steps. Structural characterization is carried out by surface area measurement according to Brunauer-Emmet-Teller (BET), X-ray diffraction (XRD), scanning electron microscopy (SEM) and static laser scattering (SLS). Excellent electrical conductivity is demonstrated. The use of ATO cathodes in Li-$O_2$ batteries leads to an unprecedented and potentially beneficial cell chemistry involving the formation of $Li_2O$. This provides new mechanistic insights and implications for cathode design concepts that might enable the reversible cycling of Li-$O_2$ cells.

## Experimental

***Synthesis of conductive ATO nanoparticles.***—In the procedure adapted from Zhang and Gao,[39] a mixture of metallic tin and $Sb_2O_3$ is first dissolved in nitric acid, which converts the metal cations to their highest oxidation states, $Sn^{4+}$ and $Sb^{5+}$. According to the Pourbaix diagrams for Sn and Sb,[40] this process requires the careful adjustment of the pH to a final value between −0.7 and 0.2. At positive potentials (i.e., under oxidizing conditions), both $Sb_2O_5$ and $SnO_2$ are precipitated in this pH range. A higher pH would lead to the sole precipitation of $SnO_2$, whereas a lower pH would leave both cations in solution. Ideally, the pH is set so that during oxidation and dissolution of the precursors it rises from an initial value below −0.7 to a value between −0.7 and 0.2 to allow a well-defined coprecipitation. Furthermore, tin is used in granulated form instead of a powder to slow down the dissolution of tin in comparison to antimony oxide.

In a typical synthesis, 30 ml of concentrated $HNO_3$ (69 wt%, puriss. p.a., Sigma Aldrich, USA) are added to 50 ml deionized water in an open 100 ml PTFE autoclave liner. 2000 mg (16.85 mmol) granulated Sn (≥99.5%, Sigma Aldrich, USA) and 129 mg (0.44 mmol) $Sb_2O_3$ powder (≥99.9%, Sigma Aldrich, USA) (molar ratio Sb/Sn = 5/95) are at once added under vigorous stirring, leading to a noticeable $NO_2$ release and the formation of a yellowish colloid. After 10 minutes, the autoclave (HighPreactor BR-100, Berghof, Germany) is sealed, heated to 140°C at 2 K/min, held at 140°C for 10 h and passively cooled down to RT overnight. The resulting bluish powder is separated from the liquid phase by centrifugation, washed repeatedly with deionized water until the washing water reaches a pH of 6, then washed with ethanol once and dried in static air at 70°C overnight.

Calcination of dry powders is conducted in a tube furnace (Carbolite, Germany) in a gas flow of 20% $O_2$ (99.999%, Westfalen, Germany) in Ar (99.999%, Westfalen, Germany) at a flowrate of 400 ml/min. Samples are heated to 600°C at 5 K/min, held at 600°C for 3 h, then passively cooled to RT in the furnace.

Calcined samples are ground in a planetary ballmill (Pulverisette 7 Premium Line, Fritsch, Germany). Therefore, 1 g of sample is suspended in 3 ml isopropanol. The suspension is poured into a 20 ml $ZrO_2$ milling jar containing 10 $ZrO_2$ balls (Ø 10 mm). Milling is conducted at 200 rpm over 6 cycles of 10 min milling time each and 1 min pause between cycles. The product is then separated from the solvent by centrifugation and dried at 70°C in static air overnight.

***Structural characterization techniques.***—Surface area measurements are performed on a gas sorption analyzer (Autosorb-iQ, Quantachrome, USA) at 77 K using nitrogen as adsorbent. Samples are pretreated at 140°C for 15 h (as-synthesized ATO) or 350°C for 3 h (calcined ATO) under vacuum. Adsorption isotherms are recorded in the relative pressure range of 0.05 ≤ (p/$p_0$) ≤ 0.30 and used to calculate BET surface areas.

X-Ray Powder Diffraction data are collected using a diffractometer (Stadi MP, STOE, Germany) equipped with a one-dimensional silicon strip detector (Mythen 1K, Dectris, Switzerland) and monochromatized Mo ($K_{\alpha 1}$) radiation (λ = 0.7093 Å, 50 kV, 40 mA) in Debye-Scherrer geometry using a 0.7 mm diameter glass capillary as sample holder. Data is collected between 2° and 58° (2θ) with a resolution of 0.015°; the overall data-collection time is set to 30 min.

Agglomerate size determination via static laser scattering (SLS) is conducted on a particle size distribution analyzer (LA-950V2, Retsch, Germany). 10 mg material are dispersed in 10 ml isopropanol by ultrasonification. A variable amount of this dispersion is added to a stirred ethanol stock solution in the instrument's sample cuvette, thus adjusting the degree of absorption of the instrument's laser beams by the dispersion. Refractive indexes of Indium-doped tin oxide in ethanol (n(650 nm) = 1.8, n(405 nm) = 2.1) are used for particle size calculations.

SEM images are recorded on a scanning electron microscope (NEOSCOPE JCM-6000, JEOL, Japan). For sample preparation, the particles are distributed homogeneously on a conductive carbon tape from the isopropanol dispersions initially used in the SLS experiments (see above).

***Powder conductivity measurement.***—400 mg of sample is pressed into a pellet of 6 mm Ø with an applied pressure of 400 kg (approx. 1400 bar) using a hydraulic pellet press (PE-011, Mauthe, Germany) and a pressing tool made in-house. The tool features an electrically insulating polyoxymethylene (POM) cylinder with an axial drill hole, a stainless steel (SS) bottom part and a SS stamp. The upper part of the stamp is of 15 mm Ø and travels directly in the drill hole for precise vertical alignment, whereas the lower part is of 6 mm Ø and travels in a PE tube that fits inside the lower part of the drill hole. The sample is placed inside the PE tube and is pressed between the SS bottom and stamp. The height of the pressed pellet (typically 3–4 mm) can be read from the vertical position of the stamp in the POM cylinder. Bottom and stamp are electrically insulated against the pellet press by POM sheets, and are connected to a potentiostat (VMP3, Bio-Logic, France) in a 2-point probe setup. Voltages of 1, 2, 4 and 8 mV are applied for 5 minutes each, and the resulting currents are recorded. Electrical conductivities are calculated from the electrical resistance and the geometric measures of the pellet.

***Electrode preparation, Li-$O_2$ cell assembly and cycling.***—ATO-based electrodes are prepared by ultrasonication of 300 mg ATO in isopropanol and subsequent addition of PTFE binder (PTFE micropowder, 3M, USA) with a binder-to-active material ratio of 5/95. The resulting ink is mixed in a planetary orbital mixer (Thinky, USA) for 5 min at 2000 rpm. The solvent is evaporated at room temperature and the obtained viscous paste is pressed into pre-punched SS meshes of 15 mm Ø using a spatula (SS mesh with quadratic windows of 190 μm edge length and wires of 65 μm diameter, Spörl OHG,

Germany). The mesh serves as both a conductive grid and a mechanical support. Vulcan carbon-based electrodes are prepared analogous, with a binder-to-active material ratio of 10/90. Coated mesh electrodes with ATO loadings of $23 \pm 5$ mg/cm$^2$ and carbon loadings of $2.7 \pm 0.5$ mg/cm$^2$ are dried at 120°C for 12 h in a vacuum glass oven (Büchi, Switzerland) and directly transferred to an Ar-filled glove box (H$_2$O < 0.1 ppm, O$_2$ < 0.1 ppm, MBraun, Germany). Li-O$_2$ cells are assembled inside the glove box using an ATO-based cathode (Ø 15 mm), a Li anode (Ø 17 mm), two Celgard C480 separators (Ø 28 mm) and 120 µL of electrolyte. The electrolyte consists of 0.5 M LiTFSI (lithium bis-(trifluoromethanesulfonyl)-imide, Sigma Aldrich, 99.95% metal basis, vacuum dried at 150°C for 24 hours before use) in diglyme (diethylene glycol dimethyl ether, 99.5%, Sigma Aldrich, purified by fractional distillation over metallic sodium, dried over Sylobead MS 564C zeolites (3 Å, Grace Devision) and verified to contain < 5 ppm water as determined by Karl Fischer titration (Titroline KF, Schott Instruments, Germany)). Cells are purged with O$_2$ for 60 s and cycled at a rate normalized to the active material's surface area of 0.086 µA/cm$^2_{BET}$. In case of the formation of a surface film consisting of electrically insulating discharge products as expected for Li air cells, the surface that is accessible to the electrolyte is the capacity-controlling parameter.[19] Consequently, applying a surface-normalized rate is considered as a much more suitable basis to compare different materials than a mass-normalized rate. Our applied rate equals 45 mA/g$_{ATO}$ (A$_{BET}$ of ATO is 50 m$^2$/g, primary particles are non-porous and therefore the surface area is largely unaffected by the PTFE binder) or 120 mA/g$_{carbon}$ (A$_{BET}$ of Vulcan carbon in electrodes including PTFE binder and after subtraction of surface area in micropores is 137 m$^2$/g[19,16]).

***Quantification of the Li$_2$O$_2$ and Li$_2$O content of ATO electrodes at different states of charge.***—ATO cathodes from Li-O$_2$ cells in different states of charge are analyzed to quantify their Li$_2$O$_2$ and Li$_2$O content. ATO cathodes are removed from the cells in an Ar-filled glove box, dried for 12 h at RT in a vacuum glass oven (Büchi, Switzerland) and then dispersed in defined amounts of ultra-pure deionized water (Millipore, $\rho$ > 18 MΩ · cm). Due to the excess of water Li$_2$O$_2$ is entirely converted to LiOH and H$_2$O$_2$:

$$Li_2O_2 + 2H_2O \rightarrow 2LiOH + H_2O_2 \qquad [3]$$

The formed H$_2$O$_2$ is then quantified as described in our previous work.[36] Therefore, the dispersion is filtered to remove residual ATO, then a defined amount of Titanium(IV) oxysulfate solution (1.9–2.1% for determination of hydrogen peroxide (H 15), according to DIN 38 409, part 15, DEV-18, Sigma-Aldrich) is added. Then the absorbance of the formed yellow [Ti(O$^{2-}$)]$^{2+}$ complex is measured by UV-vis spectroscopy (Lambda 35, Perkin Elmer, USA). Results are quantified using a reference absorbance curve derived from several defined amounts of commercial Li$_2$O$_2$ which were dissolved in H$_2$O, converted to H$_2$O$_2$ and treated according to DIN 38 409 as described above. The Li$_2$O$_2$ content of commercial Li$_2$O$_2$ (technical grade, >90%, Sigma Aldrich, USA) was determined by thermogravimetric analysis to be 92.8%, as described previously.[8] Error calculations include the standard error of slope and intercept of the calibration curve as well as the instrument's error of an absorbance of 0.005.

By dispersing ATO cathodes in water, not only Li$_2$O$_2$ but also Li$_2$O is entirely converted to LiOH:

$$Li_2O + H_2O \rightarrow 2LiOH \qquad [4]$$

The total amount of LiOH is quantified by titration with an aqueous solution of HCl using methyl red as an indicator while purging the titrant solution with argon to avoid dissolution of atmospheric CO$_2$. It has to be noted that not only dissolved CO$_2$ from the atmosphere, but also CO$_3^{2-}$ from Li$_2$CO$_3$, and partly CH$_3$COO$^-$ and CHOO$^-$ from CH$_3$COOLi and CHOOLi would add to the titrated amount of LiOH, whereas H$_2$O$_2$ does not affect the titration result (see Fig. S1 in the SI). Hence, the cumulative amount of Li$_2$O, LiOH, Li$_2$CO$_3$, CH$_3$COOLi and CHOOLi can be determined as the difference of the amount of

LiOH and other basic or weakly acidic species obtained from titration, and the amount of H$_2$O$_2$ determined by UV-vis (from Li$_2$O$_2$ only).

As will be shown later, the formation of significant amounts of LiOH, Li$_2$CO$_3$, CH$_3$COOLi and CHOOLi during discharge can be excluded by attenuated total reflection fourier transform infrared spectroscopy (ATR-FTIR) analysis (Spectrum 2, Perkin Elmer, USA, equipped with a diamond ATR) of discharged electrodes, as all mentioned compounds possess intense characteristic IR absorption bands. Consequently, the amount of Li$_2$O in discharged electrodes corresponds to the difference of titration and UV-vis results.

***Gas analysis with pressure transducer and on-line electrochemical mass spectrometer (OEMS).***—For the in-situ gas analysis during discharge and charge of the Li-O$_2$ battery with ATO-based cathodes and Vulcan carbon cathodes, a coupled system with a direct pressure/vacuum capacitance manometer (Baratron, MKS instruments, in the following referred to as "Baratron")[41] and our On-line Electrochemical Mass Spectrometer (OEMS)[42] is used (Figure 1).

The OEMS cell is equipped with a capillary leak connected to the OEMS (E) and two valves (A and B) for gas flushing, one of which (A) is connected to the gas line and the second one to the vacuum pump (B). The Baratron is connected to the OEMS cell by a $\frac{1}{4}$'' stainless steel tubing. The measurement procedure with the coupled gas analysis system first involves the OEMS cell assembly inside an Ar-filled glove box (H$_2$O < 0.1 ppm, O$_2$ < 0.1 ppm). Subsequently the cell is connected to the pressure transducer unit using cutting-ring fittings (VCR). The whole assembly is then joined to a vacuum pump and first the pressure transducer unit (volume V$_B$) and the connecting unit (V$_T$) are evacuated (valves C and D open, valves A, B and E closed) for 10 min. After connecting the cell to the gas line, the connection between Baratron and OEMS cell is opened such that the Ar gas in the cell head space expands to the whole system (V$_B$ + V$_T$ +V$_C$; valves B and C open, valves A, D, and E closed). Then the whole system is flushed with O$_2$ (99.999%, Westfalen, Germany) for 2 min at a flowrate of 80 sccm (valves A-D open, valve E closed). After that the O$_2$-filled cell is discharged while recording the O$_2$ consumption as a pressure decrease with the Baratron (valves B and C open, valves A, D, and E closed). As soon as the discharge to 2 V vs. Li/Li$^+$ is finished, the whole system is flushed with Ar to remove the remaining O$_2$ (valves A-D open, valve E closed) and to have a pure Ar background for monitoring the gas evolution during charge by OEMS. During charge only gases from the cell head space are sampled by OEMS through the capillary leak (valve E open, valves A-D closed).

## Results

***Synthesis and characterization of ATO nanoparticles with high conductivity and high surface area for electrode preparation.***—Our aim is to produce ATO nanoparticles suitable for electrode preparation, i.e. possessing an adequate electrical conductivity of $\geq 10^{-1}$ S/cm combined with the highest possible surface area to enable high capacities, a moderate agglomerate size of $\leq 20$ µm suitable for the fabrication of smooth electrode coatings, and no contamination by organic residues or chloride which likely would compromise cell performance. To pursue this goal, we apply a hydrothermal synthesis of ATO nanoparticles from chlorine-free precursors using a modified procedure first reported by Zhang and Gao,[39] followed by additional calcination and milling steps. An Sb-doping level of 5 mol% is chosen on the basis of both theoretical and experimental data in the literature: Doping levels of 2–7 mol% Sb should lead to degenerate semiconductors with metallic properties ([43] and sources therein), and ATO nanoparticles with doping levels of 4–10 mol% Sb have been reported to give optimum electrical conductivity.[44,30] Further, a high Sb$^{5+}$/Sb$^{3+}$ ratio[43] and low Sb surface segregation[30] are required to create n-type conductivity.

X-ray diffraction patterns of as-synthesized, calcined, and ballmilled ATO samples have been recorded to provide detailed
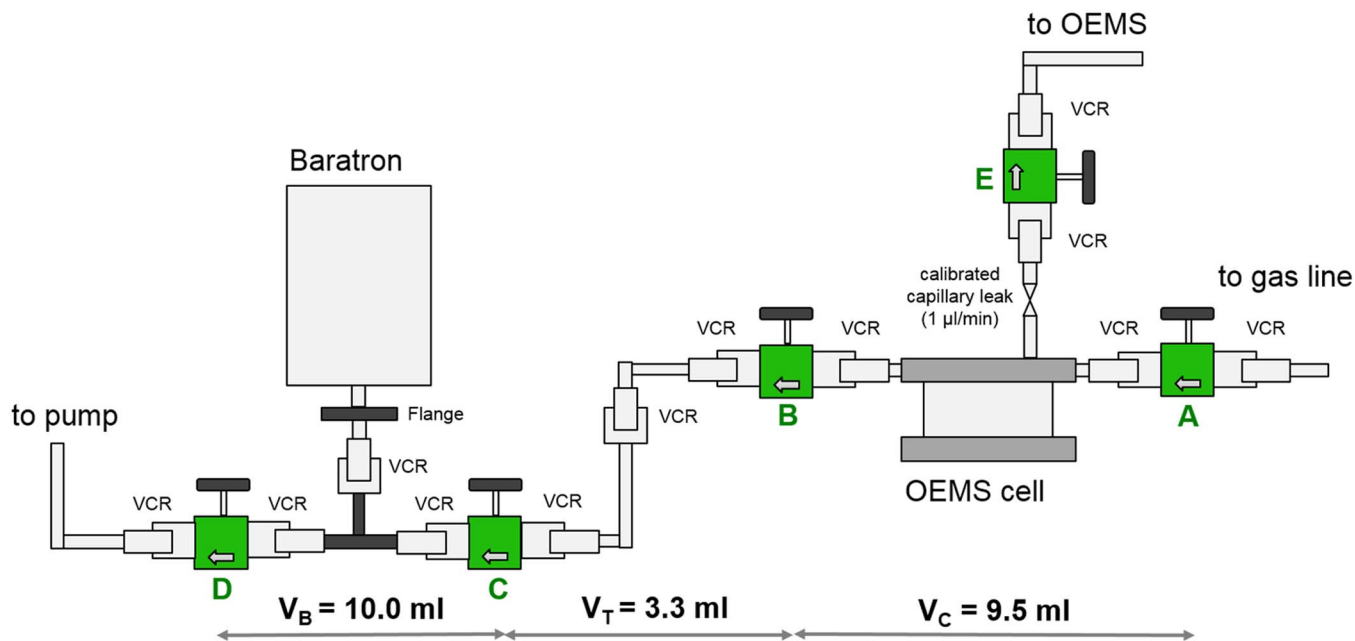
**Figure 1.** Configuration of the coupled system gas analysis of ATO cells with a Baratron pressure transducer and OEMS with $V_B \equiv$ volume of the Baratron pressure transducer unit, $V_T \equiv$ volume of the connecting unit, and $V_C \equiv$ volume of the cell unit. VCR refers to a connection with cutting ring fitting.

information on the crystal phases and the degree of crystallinity of the materials, as shown in Figure 2.

The diffraction patterns of all measured samples are in excellent agreement with the casserite structure of antimony-doped tin oxide with a chemical composition of $Sn_{0.938}Sb_{0.062}O_{1.88}$.[45] This corresponds well to our target Sb doping level of 5 mol%, thus confirming the successful doping of the host lattice during the hydrothermal synthesis
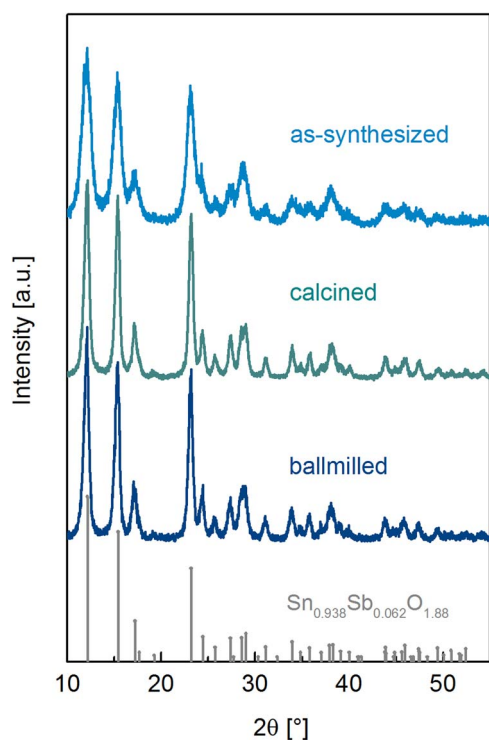
and the absence of any phase separation during post-synthetic treatments. The as-synthesized sample consists of crystalline domains of ∼5 nm $\emptyset_m$ (calculated from the FWHM of the reflection at 12° 2θ). The XRD-derived crystallite size increases to ∼13 nm $\emptyset_m$ upon calcination, and remains unchanged during ballmilling.

All ATO samples are further analyzed by electrical conductivity measurements, BET and SLS to investigate the decisive properties for electrode preparation. The results are summarized in Table I.

The ATO nanoparticles obtained from hydrothermal synthesis only possess an electrical conductivity of $5 \cdot 10^{-4}$ S/cm. This is contradictory to the results of Zhang and Gao,[39] who claim that this hydrothermal route yields highly conductive ATO nanoparticles without any further thermal treatment, which would indeed set it apart from other methods that are generally reported to require calcination temperatures above 500°C[43,44] to yield highly conductive materials. However, the BET surface area of 190 m²/g is in good agreement with the data published by Zhang and Gao. The mean primary particle diameter calculated from BET (assuming spherical particles) of 5 nm exactly matches the mean crystalline domain size calculated from XRD patterns, confirming that the primary particles are indeed single crystalline, which is an essential prerequisite for efficient electron conduction. The maximum size of agglomerates which cannot be broken up by ultrasonication as measured by SLS is 20 μm.

Calcination of the as-synthesized ATO at 600°C enhances its conductivity by 4 orders of magnitude to 2 S/cm, which easily meets the requirements for electrodes and puts our results in line with the general trend for the conductivity of ATO reported in literature. The



**Figure 2.** XRD patterns (Mo (K$_{\alpha 1}$) radiation) of ATO as-synthesized, calcined at 600°C in air and ball milled. Reference diffraction pattern of the casserite structure of $Sn_{0.938}Sb_{0.062}O_{1.88}$.[49]

**Table I. Impact of post-synthetic treatments on ATO conductivity ($\rho_{powder}$), BET surface area ($A_{BET}$), BET-derived particle size ($\emptyset_{m, BET} = 6/[\rho_{ATO} \cdot A_{BET}]$), XRD-derived particle size ($\emptyset_{m, XRD}$), and average agglomerate diameter ($\emptyset_{max, SLS}$).**

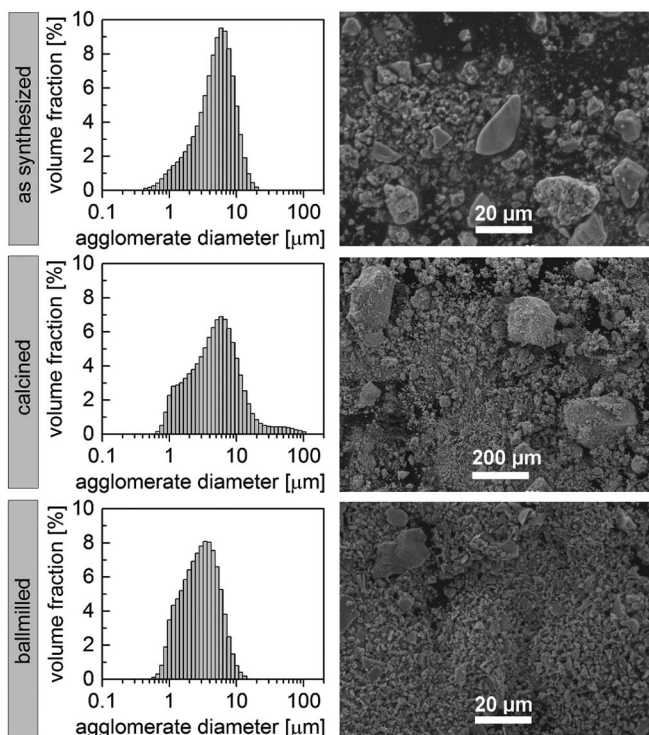| ATO | $\rho_{powder}$ [S/cm] | $A_{BET}$ [m²/g] | $\emptyset_{m, BET}$ (particles) [nm] | $\emptyset_{m, XRD}$ (crystallites) [nm] | $\emptyset_{max, SLS}$ (agglomerates) [μm] |
|---|---|---|---|---|---|
| as synthesized | $5 \cdot 10^{-4}$ | 190 | 5 | 5 | 20 |
| calcined | 2 | 50 | 17 | 13 | 200 |
| ballmilled | 2 | 50 | 17 | 13 | 15 |

**Figure 3.** Agglomerate size distributions obtained by SLS (left panel) and SEM images (right panel) of ATO as synthesized (top), calcined at 600°C in air (mid) and after ballmilling (bottom). Note the different magnifications indicated by the scale bars of the SEM images.

increase in conductivity is attributed to both crystal growth and fusing of primary particles, lowering the number and increasing the contact area of interfaces between particles and thus lowering electrical resistance. As expected due to crystal growth and sintering, the BET surface area decreases from 190 m$^2$/g to 50 m$^2$/g during calcination. The corresponding particle size of 17 nm agrees reasonably well with the crystallite size of 13 nm calculated from XRD. This surface area still exceeds that of most reported ATO's with comparable conductivities, and is sufficient to enable high capacities. However, calcination also leads to increased agglomerate sizes of up to 200 μm, thus preventing the direct preparation of smooth electrode films of ∼130 μm thickness from calcined ATO.

Accordingly, a low-energy wet-ballmilling procedure was applied, resulting in a maximum agglomerate size of 15 μm while electrical conductivity, BET surface area and crystallite size remain unchanged compared to the calcined product. This suggests that ballmilled ATO is fully suitable for the use as cathode material in Li-O$_2$ cells.

Figure 3 gives a complete overview of the agglomerate size distributions (SLS) and textures (SEM) of the as-synthesized, calcined and ballmilled materials.

It can be seen that the sharp agglomerate size distribution of the as-synthesized material (volume averaged mean diameter of $\emptyset_m =$ 5.2 μm, and maximum diameter of $\emptyset_{max} \approx 20$ μm) is broadened during calcination, in particular toward the formation of few very large agglomerates ($\emptyset_m = 6.9$ μm, $\emptyset_{max} \approx 200$ μm). After ballmilling, an even narrower size distribution as the one of the as-synthesized material is obtained ($\emptyset_m = 3.4$ μm, $\emptyset_{max} \approx 15$ μm), making the texture of this material suitable for electrode preparation.

***Electrochemical cycling of ATO cells.***—The upper panel of Figure 4 shows a representative voltage profile of the first discharge-charge cycle of Li-O$_2$ cells with ATO cathodes, with marked states of charge (SOC) for the subsequent analysis of discharge products #1, #2 and #3. The lower panel of Figure 4 depicts the specific discharge
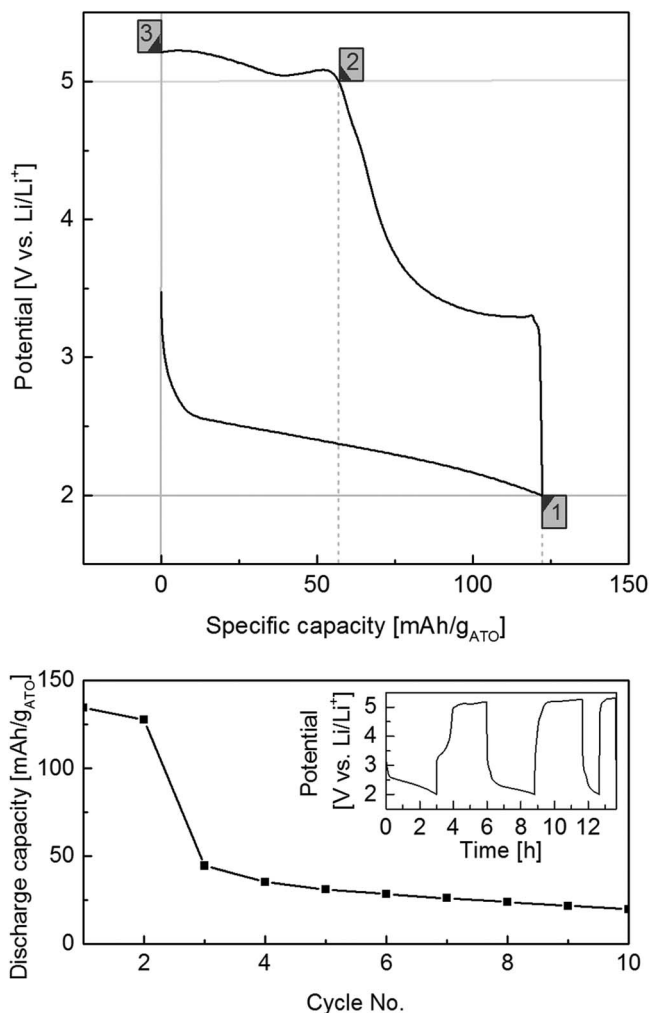


**Figure 4.** Representative voltage profile of the first cycle (upper panel), discharge capacity vs. cycle number (lower panel) and corresponding voltage profiles of cycles 1–3 (lower panel, inset) of Li-O$_2$ cells with ATO cathodes. Cells are cycled galvanostatically at a surface-normalized rate of 0.086 μA/cm$^2_{BET}$ with a lower cutoff voltage of 2.0 V and capacity-limited charging up to the previous discharge capacity. Quantification of discharge products in ATO cathodes is carried out at indicated SOC's in the first cycle: #1 discharged to 2 V, #2 recharged to 5 V, #3 recharged to 1$^{st}$ discharge capacity.

capacity as a function of cycle number, with the corresponding voltage profile for the first 3 cycles shown in the inset.

As shown in the upper panel of Figure 4, the discharge of Li-O$_2$ cells with ATO cathodes is characterized by a sloping potential rather than a plateau, starting at 2.6 V and declining with increasing steepness until the cutoff of 2.0 V is reached. First discharge capacities typically reach 110 ± 30 mAh/g$_{ATO}$ (792 ± 216 μC/cm$^2_{BET}$) (result obtained from 15 cells). Normalized to the cathode's BET surface area, first discharge capacities obtained with ATO are slightly superior to those with Vulcan carbon cathodes, which are typically at 183 ± 50 mA/g$_{Carbon}$ (474 ± 130 μC/cm$^2_{BET}$).[19] The charging initiates at a potential plateau of ∼ 3.3 V, after which the potential rises to approx. 5 V, at which point 48 ± 6% of the 1$^{st}$ discharge capacity have been recovered (result obtained from 5 cells); subsequently, a charging plateau of around 5.2 V is observed. To avoid overcharging beyond this point, capacity-limited charging is applied instead of a voltage cutoff, meaning the charge is stopped once the previous discharge capacity is recharged.

Given that only a partial recharge is possible in a potential window up to 4.7 V, the uppermost potential up to which the diglyme electrolyte is expected to be stable,[42] the rapid capacity fading within

the first 3 charge/discharge cycles ending at ∼ 5.2 V (Figure 4, lower panel) is not surprising. However, it is noteworthy that unlike cells with carbon cathodes, which exhibit an initial capacity increase over cycles 2–5 due to the formation of electrolyte degradation products that hinder passivation by $Li_2O_2$ growth,[16,19] no such effect is seen with ATO cathodes. This indicates substantial differences in the extent and/or the products of electrolyte degradation on ATO versus carbon surfaces. The striking fact that the 1st discharge capacity is almost completely recovered in cycle 2, but severely compromised in cycle 3, corresponds to the voltage rising straight up to > 4.5 V in the 2nd charge (see inset in Figure 4, lower panel), and will be further rationalized in the Section Rechargeability of discharge products.

*Identification of discharge products.*—To investigate the processes involved in the discharge and charge of ATO cells, which are expected to differ from those in cells with carbon cathodes judging from the fundamentally different voltage profiles,[16] the quantification of $Li_2O_2$ and $Li_2O$ content at different SOC is pursued using three complementary analytical methods: (i) The sum of all potential discharge products[45] such as $Li_2O_2$, $Li_2O$, LiOH and $Li_2CO_3$ (partly also Li acetate and Li formate) is determined by acid base titration (see also Fig. S1 in the SI). (ii) The amount of $Li_2O_2$ is quantified by photometric detection in the UV-vis range of a colored $[Ti(O^{2-})]^{2+}$ complex formed by the reaction of titanium(IV) oxysulfate with $H_2O_2$, which is exclusively generated by the hydrolysis of $Li_2O_2$. (iii) The absence or presence of discharge products other than $Li_2O_2$ and $Li_2O$ is verified by ATR-FTIR of discharged electrode samples by the absence of their distinct infrared absorption bands.

Figure 5 shows the ATR-FTIR spectra of fresh and discharged ATO cathodes and several reference samples (left panel), as well as the quantification of discharge products calculated from titration and UV-vis photometry (mid and right panels). The SOC used for product analysis are marked in Figure 4 as #1 discharged, #2 charged to 5 V, and #3 charged to the 1st discharge capacity. Product analyses at each SOC are taken from at least 2 different cells. All given amounts are mean values with their standard deviation (SD), taking into consideration the error propagation when subtracting (ii) from (i). To compensate for different cathode loadings in different cells, all amounts are normalized to μmol of Li per As of 1st discharge capacity of each cell. The resulting fractions of the discharge capacity that are chemically stored in each product are visualized in the mid panel of Figure 5. For the upcoming comparison with Baratron/OEMS data in the next section of this work, an additional normalization of the $Li_2O_2$ and $Li_2O$ fractions to μmol of $O_2$ equivalents contained in each product per As of 1st discharge capacity is carried out. The results reflect the fact that $Li_2O_2$ is produced by a $2e^-/O_2$ process, while $Li_2O$ is formed in a $4e^-/O_2$ reaction, and are shown in the right panel of Figure 5.

On discharged electrodes (SOC #1), the total amount of Li in the discharge products that are detected by acid base titration of LiOH is $8.90 \pm 0.64$ $\mu mol_{Li}$/(As). This equals $86 \pm 6\%$ of the total discharge capacity being chemically stored in $Li_2O_2$, $Li_2O$, LiOH and $Li_2CO_3$ (cross-sensitivity to Li acetate and Li formate to be addressed later). The residual $14 \pm 6\%$ are used up by other reactions that will be addressed later. According to UV-vis measurements, $Li_2O_2$ accounts for $4.52 \pm 0.64$ $\mu mol_{Li}$/(As) or $44 \pm 6\%$ of discharge capacity. Accordingly, the other $4.38 \pm 1.28$ $\mu mol_{Li}$/(As) or $42 \pm 12\%$ of stored capacity must represent $Li_2O$, LiOH, $Li_2CO_3$ (and possibly Li salts of electrolyte degradation products like Li acetate and Li formate).

Comparing the ATR-FTIR spectrum of a discharged electrode to the reference spectra of pure lithium salts (Figure 5, left panel), it is clear that the electrode shows no absorption bands which could be coherently assigned to LiOH ($3680$ $cm^{-1}$), $Li_2CO_3$ ($1420$ and $860$ $cm^{-1}$) or Li formate ($1590$, $1370$ and $780$ $cm^{-1}$). However, it exhibits marginal absorption bands at $1600$ and $1440$ $cm^{-1}$ indicating
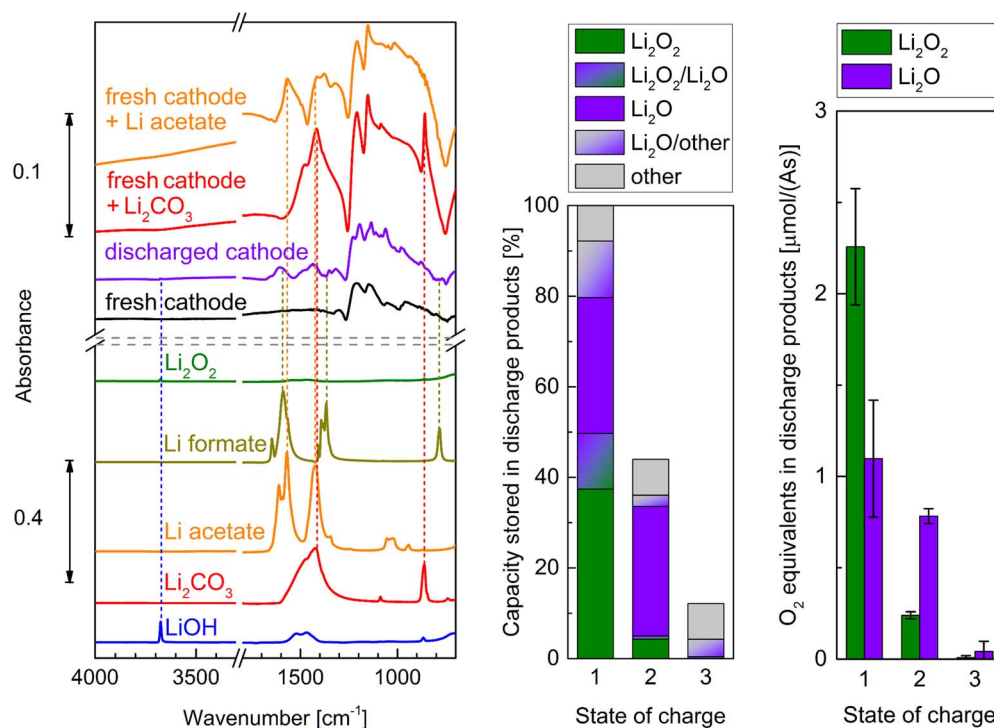


**Figure 5.** Left panel: ATR-FTIR spectra of fresh and discharged ATO cathodes and reference spectra of fresh cathode powder (ATO + binder) mixed with amounts of $Li_2CO_3$ or Li acetate that equal the claimed fraction of $Li_2O$ in ATO cathodes after the 1st discharge. Additional reference spectra of LiOH, $Li_2CO_3$, Li acetate, Li formate and $Li_2O_2$. Spectra are cut off at $700$ $cm^{-1}$, as intense ATO absorption bands mask all Li salt absorption bands below $700$ $cm^{-1}$. Mid and right panels: Quantification of discharge products in ATO cathodes at different SOC: #1 1st discharge to 2 V, #2 recharge to 5 V, #3 recharge to 1st discharge capacity. Product amounts are normalized to each cell's discharge capacity for comparison of different cells (mid panel), as well as each product's stoichiometric oxygen content for comparison with Baratron/OEMS measurements (right panel). Product amounts for each SOC are mean values and standard deviations calculated from at least 2 cells.

the presence of trace amounts of Li acetate (1570 and 1420 cm$^{-1}$). The reference spectrum of a fresh ATO electrode shows that none of the characteristic bands of any Li salt is masked by absorption bands caused by ATO or the PTFE binder. To further demonstrate the sensitivity of the ATR-FTIR measurement, additional reference spectra of samples consisting of fresh cathode material (ATO + binder) intimately mixed with $Li_2CO_3$ or Li acetate are shown. The Li salt fractions in these samples equal the claimed fraction of $Li_2O$ in a discharged electrode. This provides references for the hypothetic scenarios, if all claimed $Li_2O$ on a discharged ATO electrode were indeed $Li_2CO_3$ or Li acetate. The intensities of the resulting reference bands imply that the marginal absorption bands of the discharged electrode at 1600 and 1440 cm$^{-1}$ cannot account for a substantial amount of Li acetate, nor mask a significant amount of $Li_2CO_3$. It also has to be considered that only ∼1/3 of the present Li acetate traces are actually titrated (see Fig. S1 in the SI), so that ∼2/3 of all acetate species are part of the product fraction denoted as "other" in the mid panel of Figure 5, rather than being part of the product fraction quantified by titration. Consequently, $Li_2O$ which does not possess any characteristic IR absorption bands in the accessible range, must be the only significant discharge product quantified by titration besides $Li_2O_2$. A fraction close to 42 ± 12% of the discharge capacity is therefore claimed to go into the formation of $Li_2O$. An overview over the resulting product distribution including all error margins is given in Figure 5, mid panel.

The normalization to $O_2$ equivalents then results in the amounts of $Li_2O_2$ and $Li_2O$ shown in the right panel of Figure 5. In discharged ATO cathodes, the oxygen contained in $Li_2O_2$ and $Li_2O$ accounts for 2.26 ± 0.32 and 1.10 ± 0.32 $\mu mol_{O_2}/(As)$, respectively. This corresponds to a $Li_2O_2/Li_2O$ ratio of 67/33 in respect to oxygen content, assuming that $Li_2O_2$ and $Li_2O$ are the only discharge products (see ATR-FTIR analysis above, trace amounts of Li acetate are neglected).

Although $Li_2O$ has generally been considered as a potential discharge product in Li-$O_2$ batteries and its formation via a 4-e$^-$ process is highly desirable as it can provide twice the discharge capacity per oxygen in comparison to $Li_2O_2$, it has never been identified as a substantial discharge product in Li-$O_2$ cells to date. Instead, the yield of $Li_2O_2$ in cells with carbon cathodes usually amounts to 84–91% (SI of[46]). The rest has been identified as or attributed to Li carbonate, acetate, formate and fluoride.[46] We assume that the formation of $Li_2O$ is exclusive to carbon-free support materials and likely to metal oxide surfaces, and is shown here for the first time on ATO.

***Rechargeability of discharge products.***—The charging potential consists of three distinct regions: (i) a first plateau around 3.3 V, (ii) a sloping potential until ∼5 V and (iii) a second plateau around 5.2 V. Product analyses during charge will be discussed using the amounts normalized to $O_2$ equivalents as shown in the right panel of Figure 5 in order to facilitate the comparison with the OEMS data presented in the next section.

$Li_2O_2$ is almost completely removed from the electrode surface at potentials below 5 V: Out of 2.26 ± 0.32 $\mu mol_{O_2}/(As)$ at SOC #1, only 0.24 ± 0.02 $\mu mol_{O_2}/(As)$ remain on the electrode at SOC #2, thus 2.02 ± 0.34 $\mu mol_{O_2}/(As)$ are removed. For $Li_2O$, these numbers are more ambiguous: Out of 1.10 ± 0.32 $\mu mol_{O_2}/(As)$ at SOC #1, 0.77 ± 0.04 $\mu mol_{O_2}/(As)$ are still present at SOC #2, which translates to 0.33 ± 0.36 $\mu mol_{O_2}/(As)$ being removed. Although it is clear that a fundamental fraction of $Li_2O$ remains on the electrode surface, anything between zero and half of the initial amount could be removed considering the error of measurement. According to these findings, a total of 2.35 ± 0.70 $\mu mol_{O_2}/(As)$ of oxygen should be generated during charging to SOC #2. This is to be confirmed by OEMS analysis in the following section.

During recharge to the cell's 1$^{st}$ discharge capacity, i.e. covering the charging plateaus around 3.3 and 5.2 V, all discharge products are almost completely decomposed: 0.01 ± 0.01 $\mu mol_{O_2}/(As)$ of $Li_2O_2$ and 0.04 ± 0.05 $\mu mol_{O_2}/(As)$ of $Li_2O$, so virtually no $Li_2O_2$ and no or very few $Li_2O$, are found on the electrode surface at SOC #3. Again, the total of 1.01 ± 0.06 $\mu mol_{O_2}/(As)$ that should be generated by these reactions is to be confirmed by OEMS in the following section.

The differences in the amounts of $Li_2O$ at SOC #2 and #3 clearly indicate that $Li_2O$ gets recharged during the second charging plateau around 5.2 V, whereas the possibility of a partial recharge at lower potentials has to be further evaluated by OEMS. This finding is remarkable, because according to our own observations with $Li_2O$-prefilled carbon cathodes, $Li_2O$ would not be rechargeable at all on a carbon support without catalyst.[15] However, we are aware that the comparison of nanometric films formed during discharge with the micrometer-sized particles in prefilled electrodes used in study[15] is of limited validity.

As $Li_2O_2$ and $Li_2O$ are almost completely recharged in the first charging cycle, it can be anticipated that the 2$^{nd}$ discharge starts from a relatively blank electrode surface. Therefore, it is not surprising that the 2$^{nd}$ discharge capacity is similar to the 1$^{st}$ (see Figure 4, lower panel). However, a charging process that partly takes place at potentials beyond 5 V must ultimately lead to electrolyte degradation and cell failure. This becomes manifest in the 2$^{nd}$ charge, where the potential rises straight up to > 4.5 V. This indicates that entirely different processes prevail during the 2$^{nd}$ charge, and the insulating lithium salts produced during the 2$^{nd}$ discharge mostly remain on the electrode surface. In accordance with literature,[19,20] this prevents additional lithium salt deposition in the 3$^{rd}$ discharge, which results in the major capacity drop shown in the lower panel of Figure 4. It is thus clear that the charging potential of $Li_2O$ has to be reduced substantially to create a practically rechargeable cell.

***Gas analysis of Li-$O_2$ cells with Vulcan Carbon- and ATO-based cathodes.***—For comparison and to validate the novel coupled Baratron/OEMS system, the first measurement is performed with Li-$O_2$ cells containing Vulcan Carbon cathodes (Figure 6).

During the discharge in $O_2$ atmosphere (upper panel left side until SOC #1), the $O_2$ pressure measured by Baratron decreases linearly (middle panel left side). In the subsequent charge under Ar atmosphere an almost linear increase of the $O_2$ signal (m/z = 32) can be determined by OEMS (see middle panel in Figure 6). The continuous consumption and evolution of $O_2$ correspond well to the observed voltage plateaus during discharge and charge. As the potential rises above 4.5 V toward the end of charge, oxygen evolution ceases and a significant amount of $CO_2$ is detected (see SOC #2 in upper panel). The voltage plateau around 4.7 V after completion of the charging process (right panel in Figure 6) is attributed to electrolyte decomposition, accompanied by the formation of $H_2$.

The gas consumption and evolution measurements by pressure transducer and OEMS are used for the calculation of current-normalized gas evolution rates (lower panel in Figure 6). This allows to distinguish between different reduction and oxidation processes in the cell. Taking Faraday's constant (96485 As/mol), an oxygen consumption/evolution rate of 5.18 $\mu mol/(As)$ corresponds to the formation/decomposition of $Li_2O_2$ in a two-electron process (see Equation 1). Similarly, an oxygen consumption/evolution rate of 2.59 $\mu mol/(As)$ equals a four-electron process such as the formation/decomposition of $Li_2O$ (see Equation 2) or $Li_2CO_3$:

$$4Li^+ + O_2 + CO_2 + 4e^- \leftrightarrows 2Li_2CO_3 \qquad [5]$$
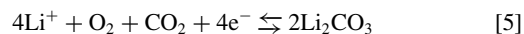
The latter can be distinguished by an additional consumption/release of $CO_2$, whereby consumed $CO_2$ does not have to be present in the gas phase but rather originates from the simultaneous oxidation of the electrolyte and/or the carbon support.

As shown in the mid and lower panels of Figure 6, the derivative of the linear pressure decrease during discharge as measured by Baratron corresponds to a mean oxygen consumption rate of 2.17 e$^-$/$O_2$, or a ratio of 92/8 between the 2e$^-$ process product $Li_2O_2$ and 4e$^-$ process products like $Li_2O$ or $Li_2CO_3$. Consequently, the formation of $Li_2O_2$ as the main discharge product is superimposed by simultaneous 4e$^-$ processes, most likely the known $Li_2CO_3$ layer formation on carbon cathodes.[21,22]
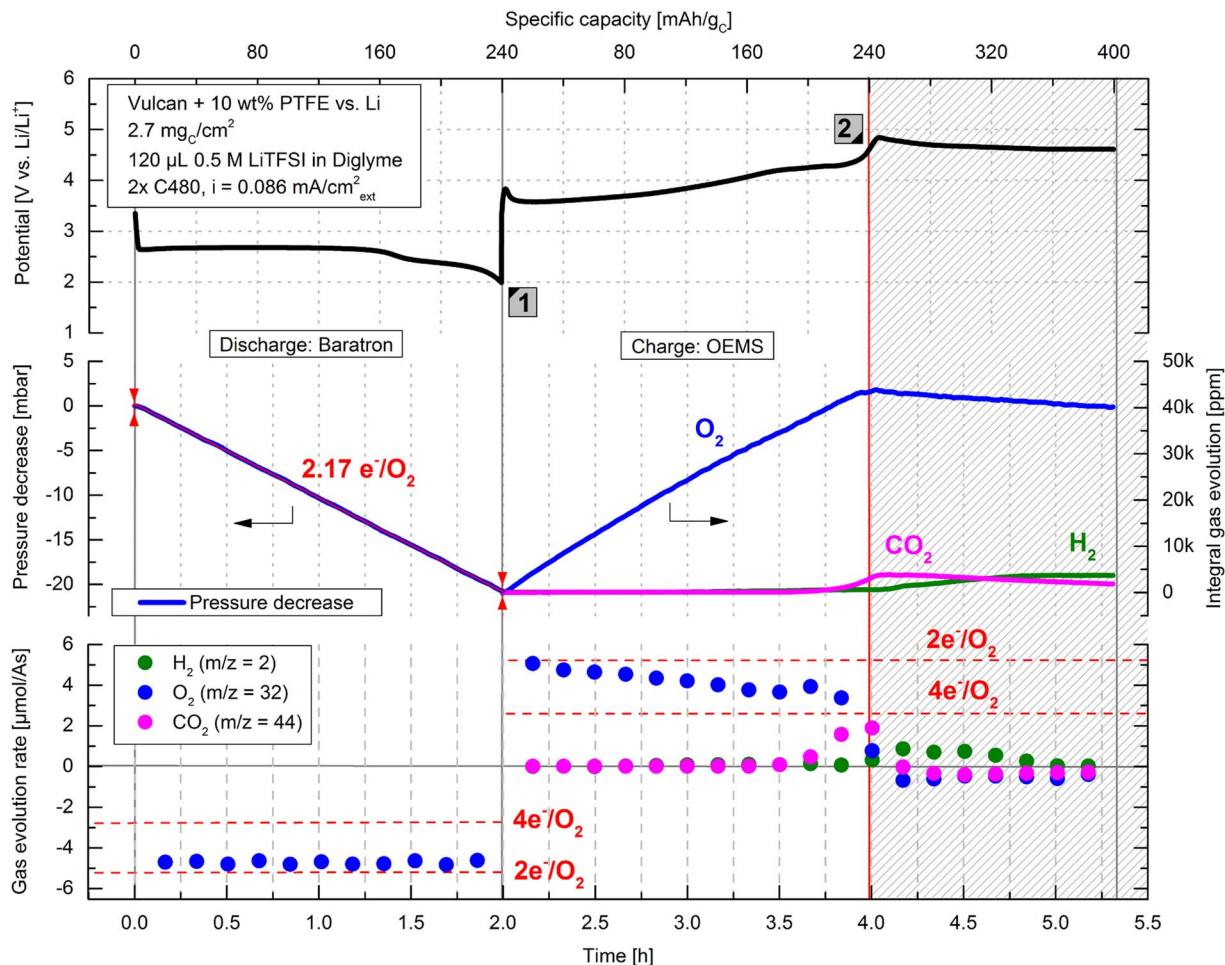
**Figure 6.** Discharge/charge profile of a Li-O$_2$ cell with Vulcan carbon cathode (upper panel), coupled with a Baratron pressure transducer during discharge in O$_2$ (mid panel left side) and evolved gas analysis by OEMS during charge in Ar (mid panel right side). Gas consumption and evolution rates calculated from pressure decrease during discharge (lower panel left side) and OEMS during charge (lower panel right side).

In the main fraction of the charge (until ∼ 4.5 V, see SOC #2 in Figure 6), O$_2$ is evolved at a rate that initially corresponds to 2e$^-$/O$_2$ and gradually decreases toward 4e$^-$/O$_2$. This indicates that the oxidation of Li$_2$O$_2$ (2e$^-$/O$_2$) is increasingly superimposed by the consumption of the formed O$_2$ in the partial oxidation of the electrolyte. As the potential rises above 4.5 V toward the end of charge, oxygen evolution ceases and a significant amount of CO$_2$ is detected. CO$_2$ evolution can be due to the re-oxidation of the Li$_2$CO$_3$ layer[15] and/or the oxidation of either electrolyte or carbon.[13,46] However, the oxidation of the carbon support has been shown to add only a minor contribution to the overall CO$_2$ evolution.[13] The oxidation of Li$_2$CO$_3$ has been shown to not result in the additional evolution of O$_2$, which is counter-intuitive given the probable anodic decomposition pathway of the compound (see Equation 5).[13,15,47] Instead, Li$_2$CO$_3$ oxidation exclusively yields CO$_2$, indicating that the generated oxygen species instantly react with the electrolyte to form additional CO$_2$.[15] The voltage plateau around 4.7 V after completion of the charging process is attributed to electrolyte decomposition, accompanied by the characteristic formation of H$_2$. In a recent study we attributed the H$_2$ evolution to the crosstalk between the electrodes, namely the diffusion of protic electrolyte decomposition species to the metallic lithium counter-electrode and their subsequent reduction.[48] As no O$_2$ can be formed anymore once the charging process is complete, it is not surprising that the O$_2$ evolution rate is slightly negative as it is being consumed by electrolyte oxidation.

To obtain information about the reversibility of O$_2$ consumption/evolution during discharge/charge, we can calculate the moles of O$_2$ in both cases. The pressure decrease of 20.7 mbar during discharge means that 19.02 μmol O$_2$ are consumed. The concentration of O$_2$ in the OEMS cell at end of charge is 43290 ppm (= 4.3% of the total 9.5 ml cell head space), which corresponds to 17.13 μmol. Accordingly, 90% of the O$_2$ consumed during discharge are again released during charge. This indicates that almost the entire amount of Li$_2$O$_2$, which contains 92% of the oxygen consumed during discharge (from above considerations on ratio of 2e$^-$ to 4e$^-$ processes), is recharged. Regarding the other 8% of consumed oxygen that is bound in Li$_2$CO$_3$, the integral value for CO$_2$ evolution at the end of the charging process is 3700 ppm, which corresponds to 1.45 μmol or 8% of consumed gases being released as CO$_2$. These numbers are in excellent agreement with a product distribution of Li$_2$O$_2$/Li$_2$CO$_3$ of 92/8, confirming that no Li$_2$O is formed on carbon cathodes.

The coupled gas analysis for ATO-based Li-O$_2$ cells, which was performed in the same way as for Vulcan carbon, is presented in Figure 7.

Despite the sloping discharge potential, the gas consumption during discharge proceeds nearly linearly (left side in Figure 7). It differs substantially from that observed with carbon cathodes since the rate is in between a two- and a four-electron process, suggesting that both the formation of Li$_2$O$_2$ and Li$_2$O are taking place simultaneously, assuming that all consumed oxygen is used for the formation of discharge products and formation of Li$_2$CO$_3$ can be neglected as demonstrated by ATR-FTIR. In the initial 45 min of discharge the O$_2$ consumption rate calculated from the linear pressure decrease corresponds to 2.72 e$^-$/O$_2$. After that the discharge proceeds at an O$_2$ consumption
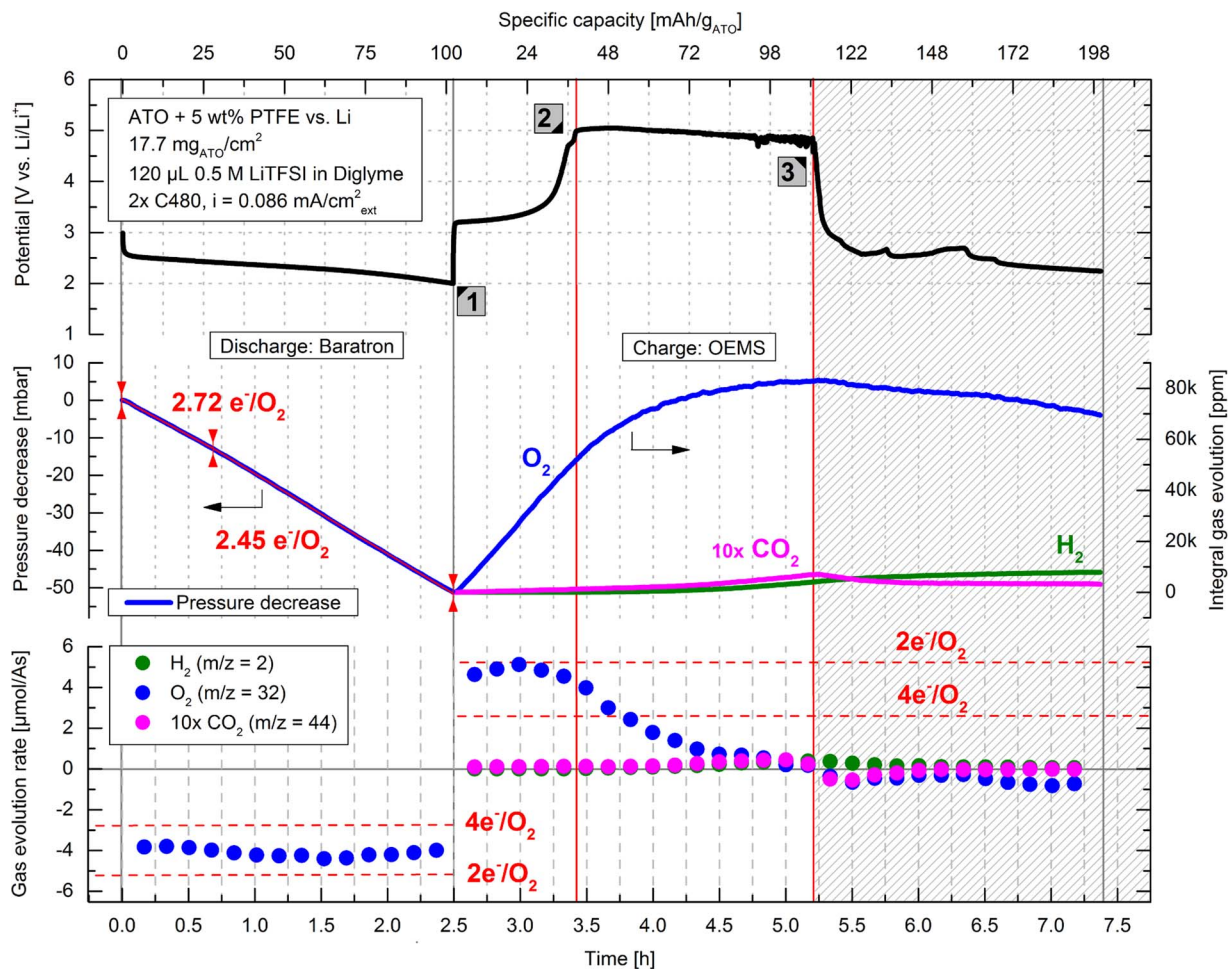
**Figure 7.** Discharge/charge profile of a Li-$O_2$ cell with ATO cathode (upper panel), coupled with a Baratron pressure transducer during discharge in $O_2$ (mid panel left side) and to evolved gas analysis by OEMS during charge in Ar (mid panel right side; note that the $CO_2$ signal is magnified by a factor of 10). Gas consumption and evolution rates calculated from pressure decrease during discharge (lower panel left side) and OEMS during charge (lower panel right side).

rate of 2.45 e$^-$/$O_2$. This finding indicates that initially the $Li_2O_2$ to $Li_2O$ ratio is 64/36 with respect to the oxygen content, while in the remaining two thirds of the discharge the ratio is 77/23. This corresponds reasonably well to the product quantification results from the combined ATR-IR, UV-vis and titration analysis, according to which the $Li_2O_2$/$Li_2O$ ratio in discharged ATO cathodes is 67/33 with respect to the oxygen content.

During the first distinct charging voltage plateau at 3.3 V, the oxygen evolution rate is close to a two-electron process (see lower panel in Figure 7), meaning that the major reaction is the electrochemical oxidation of $Li_2O_2$. This finding complements the analysis of discharge products in the previous section, where a partial oxidation of $Li_2O$ around 3.3 V could not yet be ruled out. It also means that this process is somewhat similar to the recharge of a Vulcan carbon cathode. Upon charging to 5 V (see SOC #2 in Figure 7), 55370 ppm oxygen are evolved, which equals 1.91 µmol/(As). This number is well within the 2.35 ± 0.70 µmol/(As) expected from the product analysis in the previous section, and its being at the lower end of the predicted range is in line with the finding that $Li_2O$ is not recharged to a significant extent below 5 V.

During the second voltage plateau at 5.2 V (until SOC #3 in Figure 7), the oxygen evolution slowly decreases from a four-electron process to zero, which points at the decomposition of $Li_2O$ being increasingly superimposed by oxygen consumption due to partial oxidation of the electrolyte. Electrolyte decomposition is confirmed to proceed at similar anodic potentials by galvanostatic cycling of a reference cell under argon (result not shown). Between SOC's #2 and #3, 27650 ppm

(0.96 µmol/(As)) oxygen are detected, which is in good agreement with the 1.01 ± 0.06 µmol/(As) expected from product analysis in the previous section. Here, the number being at the lower end of the predicted range could be interpreted as a confirmation that indeed part of the produced oxygen is consumed by partial oxidation of the electrolyte. At this point it is important to note that according to our previous study with $Li_2O$-prefilled carbon cathodes, $Li_2O$ would not be rechargeable at all on a carbon support without catalyst even at the electrolyte decomposition potential.[15] While the addition of a Pt catalyst enables the electrochemical decomposition of $Li_2O$ on carbon, it proceeds without any $O_2$ evolution, indicating complete oxygen consumption by electrolyte oxidation in this case.[15]

During the entire recharge, 83018 ppm $O_2$ are evolved in the OEMS cell, which equals 32.9 µmol $O_2$, whereas the pressure loss of 51 mbar during discharge corresponds to 46.91 µmol $O_2$. Consequently, only 70% of the $O_2$ consumed during discharge is released upon charge. This is explained by parasitic reactions during discharge and charge: During discharge, only 86 ± 6% of the capacity and the consumed oxygen go into the formation of $Li_2O_2$ and $Li_2O$, 14 ± 6% oxygen being used up in side reactions. During charge, the gap between the $O_2$ that should be generated by the decomposition of $Li_2O_2$ and $Li_2O$ and the $O_2$ actually detected by OEMS is attributed to some oxygen being used up by the partial oxidation of the electrolyte. Towards the end of charge (i.e. approaching SOC #3), only marginal amounts of $CO_2$ start to evolve, indicating that $Li_2CO_3$ decomposition is negligible compared to what was observed for carbon cathodes (see Figure 6). The integral gas evolution value of 700 ppm $CO_2$ corresponds to only

0.3 $\mu$mol $CO_2$ in total, which is drastically lower than the 1.45 $\mu$mol $CO_2$ obtained in case of Vulcan carbon. This is in line with ATR-IR spectra not showing any appreciable $Li_2CO_3$ formation on the ATO surface (see Figure 5, left panel). It is also plausible, since ATO is a carbon-free support material and $Li_2CO_3$ cannot be formed in the same way as in case of Vulcan carbon electrodes. When charging beyond SOC #3, the charging curve reveals a severe drop in potential and at the same time the $O_2$ evolution rate turns negative. This phenomenon has been observed before for the oxidation of composites of Pt/C catalyst with $Li_2O$, where upon the complete oxidation of $Li_2O$ (verified by ex-situ ATR-FTIR), the potential also dropped rapidly.[15] Unfortunately, the origin of this phenomenon with Pt/C as well as with ATO in the present study is still unclear.

### Discussion

We showed that the use of carbon-free cathodes such as ATO in Li-$O_2$ cells can effectively prevent the formation of carbonates on the cathode surface (as generally observed with carbon cathodes). Instead, in addition to the common discharge product $Li_2O_2$, substantial amounts of $Li_2O$ are formed on ATO. Nonetheless, the fact that only 70% of the $O_2$ consumed during discharge is released upon charge points out that significant side reactions are taking place during discharge and charge. This effectively prevents a stable cycling behavior of the ATO cathodes investigated in this study.

In contrast to carbon cathodes, where the discharge is governed by $Li_2O_2$ formation via a $2e^-/O_2$ process at a constant potential while only a partial monolayer of $Li_2CO_3$ is formed on the carbon surface, ATO cathodes lead to the formation of comparable amounts of $Li_2O_2$ and $Li_2O$ at a sloping discharge potential. The linear pressure decrease during discharge of ATO cathodes implies that the two different processes do not take place in separate time or potential regimes, but are superimposed: $4e^-/O_2$ process ($Li_2O$ formation), $2e^-/O_2$ process ($Li_2O_2$ formation) and partial electrolyte decomposition take place simultaneously. We hypothesize the formation of islands of a $Li_2O$ monolayer (ML) on the ATO surface, and the subsequent buildup of $Li_2O_2$ layers on top of $Li_2O$ islands, while the coverage of the ATO surface with $Li_2O$ keeps spreading at the same time. Figure 8 illustrates our hypothesized product deposition mechanism on ATO (lower panel) in comparison to the widely accepted deposition mechanism on carbon[21,22] (upper panel).

The deposition of $Li_2O_2$ and $Li_2O$ will advance simultaneously, if $Li_2O$ formation is favored over $Li_2O_2$ formation on the ATO surface, but $Li_2O_2$ buildup on top of $Li_2O$ is kinetically favored over further $Li_2O$ deposition on ATO. As both products are electrically insulating, both the $Li_2O/Li_2O_2$ ratio and the discharge capacity are determined by the total thickness of the $Li_2O/Li_2O_2$ layer that provides enough electrical resistance to prevent any further deposition of $Li_2O_2$ on top. This is analogue to the widely accepted capacity limitation by $Li_2O_2$ resistivity observed for carbon cathodes.[48] The approximate layer thicknesses on discharged electrodes in ML shown in Figure 8

are calculated from the 1$^{st}$ discharge capacities of $\sim$792 $\mu$C/cm$^2_{BET}$ for ATO (from this work) and $\sim$474 $\mu$C/cm$^2_{BET}$ for Vulcan carbon.[19] With ATO, 44 and 42% of the 1$^{st}$ discharge capacity are stored in $Li_2O_2$ and $Li_2O$, respectively (see mid panel of Figure 5). With Vulcan Carbon, 92 and 8% are stored in $Li_2O_2$ and $Li_2CO_3$, respectively (see evaluation of Figure 6). We assume that 260, 300 and 150 $\mu$C/cm$^2_{BET}$ are required to form one monolayer of $Li_2O_2$, $Li_2O$ and $Li_2CO_3$, respectively. These numbers are derived from the calculated number of unit cells per cm$^2$ of electrode surface according to the lattice parameters of each salt, as described in our previous work[19] and the SI of this work. The same surface-normalized discharge rate was applied in Ref.[19] and this work to ensure comparability. Though the depicted layer thicknesses should only be regarded as rough estimations, it is most likely that the $Li_2O$ surface film on ATO is much more continuous than the partial $Li_2CO_3$ boundary layer on Vulcan carbon, whereas the average thickness of the $Li_2O_2$ layer seems to be comparable on both cathode materials. As expected at low discharge rates in glyme electrolytes under water-free conditions,[36,37] no toroidal or disc-shaped deposits of discharge products can be observed by SEM on the surface of carbon or ATO cathodes (not shown).

### Conclusions

We have established a straight forward synthesis protocol for highly conductive nano-crystalline ATO with a casserite crystal structure and a Sb doping level of 5 mol%. The employed hydrothermal synthesis uses low-cost chloride-free precursors and yields nanocrystalline ATO with a specific surface area of 190 m$^2$/g and a mean primary particle size of 4.5 nm. Subsequent calcination at 600°C in air increases the conductivity by 4 orders of magnitude to 2 S/cm, which is sufficient for an application as cathode material for Li-$O_2$ batteries. Additional low-energy wet ballmilling is suitable to break up agglomerates of several hundred micrometers formed during calcination, thus limiting the maximum agglomerate size to 15 $\mu$m. This allows us to produce smooth ATO electrode coatings with low PTFE binder content.

In aprotic Li-$O_2$ battery cells, a different discharge product distribution is obtained with ATO cathodes than with carbon cathodes. We propose that a $Li_2O$ boundary layer is formed on the ATO surface in analogy to the $Li_2CO_3$ layer formed on carbon, with $Li_2O_2$ deposited on top in one continuous discharge process.

$Li_2O_2$ and $Li_2O$ are decomposed in two consecutive charge processes at $\sim$3.3 V and $\sim$5.2 V. Although the $Li_2O$ charging potential is too high for any currently available electrolyte to withstand, future combination with catalysts that lower the $Li_2O$ charging potential without lowering the electrolyte oxidation potential may lead to a practically rechargeable cell with a potentially higher energy density than a cell producing only $Li_2O_2$.

In contrast to Li-$O_2$ cells with carbon cathodes, $CO_2$ evolution during charge is negligible even beyond 5 V if ATO cathodes are used. Thus, the total oxidation of the glyme electrolyte and the PTFE binder is less pronounced than on carbon, and any oxidation of the ATO itself is intrinsically impossible.
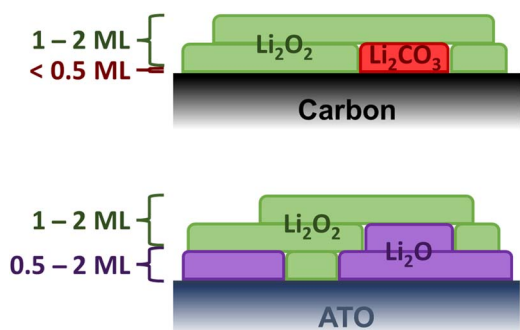
**Figure 8.** Proposed scheme of discharge product deposition on an ATO surface in analogy to the widely accepted product deposition mechanism on a carbon surface.

### References

1. K. M. Abraham and Z. Jiang, *J. Electrochem. Soc.*, **143**, 1 (1996).
2. J. Christensen, P. Albertus, R. S. Sanchez-Carrera, T. Lohmann, B. Kozinsky, R. Liedtke, J. Ahmed, and A. Kojic, *J. Electrochem. Soc.*, **159**, R1 (2012).
3. K. G. Gallagher, S. Goebel, T. Greszler, M. Mathias, W. Oelerich, D. Eroglu, and V. Srinivasan, *Energy Environ. Sci.*, **7**, 1555 (2014).

4.  G. Girishkumar, B. McCloskey, A. C. Luntz, S. Swanson, and W. Wilcke, *J. Phys. Chem. Lett.*, **1**, 2193 (2010).
5.  F. Li, T. Zhang, and H. Zhou, *Energy Environ. Sci.*, **6**, 1125 (2013).
6.  A. C. Luntz and B. D. McCloskey, *Chem. Rev.*, **114**, 11721 (2014).
7.  Y.-C. Lu, H. A. Gasteiger, M. C. Parent, V. Chiloyan, and Y. Shao-Horn, *Electrochem. and Solid State Lett.*, **13**, A69 (2010).
8.  J. Read, *J. Electrochem. Soc.*, **149**, A1190 (2002).
9.  S. S. Zhang, D. Foster, and J. Read, *J. Power Sources*, **195**, 1235 (2010).
10. Y.-C. Lu, H. A. Gasteiger, E. Crumlin, R. McGuire, and Y. Shao-Horn, *J. Electrochem. Soc.*, **157**, A1016 (2010).
11. Y.-C. Lu, E. J. Crumlin, G. M. Veith, J. R. Harding, E. Mutoro, L. Baggetto, N. J. Dudney, Z. Liu, and Y. Shao-Horn, *Sci. Rep.*, **2**, 715 (2012).
12. Y.-C. Lu, E. J. Crumlin, T. J. Carney, L. Baggetto, G. M. Veith, N. J. Dudney, Z. Liu, and Y. Shao-Horn, *J. Phys. Chem. C*, **117**, 25948 (2013).
13. B. D. McCloskey, D. S. Bethune, R. M. Shelby, G. Girishkumar, and A. C. Luntz, *J. Phys. Chem. Lett.*, **2**, 1161 (2011).
14. D. M. Itkis, D. A. Semenenko, E. Y. Kataev, A. I. Belova, V. S. Neudachina, A. P. Sirotina, M. Hävecker, D. Teschner, A. Knop-Gericke, P. Dudin, A. Barinov, E. A. Goodilin, Y. Shao-Horn, and L. V. Yashina, *Nano Lett.*, **13**, 4697 (2013).
15. S. Meini, N. Tsiouvaras, K. U. Schwenke, M. Piana, H. Beyer, L. Lange, and H. A. Gasteiger, *Phys. Chem. Chem. Phys.*, **15**, 11478 (2013).
16. K. U. Schwenke, S. Meini, X. Wu, H. A. Gasteiger, and M. Piana, *Phys. Chem. Chem. Phys.*, **15**, 11830 (2013).
17. J. Wandt, P. Jakes, J. Granwehr, H. A. Gasteiger, and R.-A. Eichel, *Angew. Chem.*, **128**, 7006 (2016).
18. H. Beyer, S. Meini, N. Tsiouvaras, M. Piana, and H. A. Gasteiger, *Phys. Chem. Chem. Phys.*, **15**, 11025 (2013).
19. S. Meini, M. Piana, H. Beyer, J. Schwämmlein, and H. A. Gasteiger, *J. Electrochem. Soc.*, **159**, A2135 (2012).
20. B. D. McCloskey, D. S. Bethune, R. M. Shelby, T. Mori, R. Scheffler, A. Speidel, M. Sherwood, and A. C. Luntz, *J. Phys. Chem. Lett.*, **3**, 3043 (2012).
21. B. D. McCloskey, A. Speidel, R. Scheffler, D. C. Miller, V. Viswanathan, J. S. Hummelshøj, J. K. Nørskov, and A. C. Luntz, *J. Phys. Chem. Lett.*, **3**, 997 (2012).
22. B. M. Gallant, R. R. Mitchell, D. G. Kwabi, J. Zhou, L. Zuin, C. V. Thompson, and Y. Shao-Horn, *J. Phys. Chem. C*, **116**, 20800 (2012).
23. M. M. Ottakam Thotiyl, S. A. Freunberger, Z. Peng, and P. G. Bruce, *J. Am. Chem. Soc.*, **135**, 494 (2013).
24. Z. Peng, S. A. Freunberger, Y. Chen, and P. G. Bruce, *Science*, **337**, 563 (2012).
25. M. M. O. Thotiyl, S. A. Freunberger, Z. Peng, Y. Chen, Z. Liu, and P. G. Bruce; *Nature Materials*, **12** 1050 (2013).
26. B. D. Adams, R. Black, C. Radtke, Z. Williams, B. L. Mehdi, N. D. Browning, and L. F. Nazar, *ACS Nano*, **8**, 12483 (2014).
27. D. Kundu, R. Black, B. Adams, K. Harrison, K. Zavadil, and L. F. Nazar, *J. Phys. Chem. Lett.*, **6**, 2252 (2015).
28. D. Kundu, R. Black, E. J. Berg, and L. F. Nazar, *Energ. Environ. Sci.*, **8**, 1292 (2015).
29. G. Zhao, R. Mo, B. Wang, L. Zhang, and K. Sun, *Chem. Mater.*, **26**, 2551 (2014).
30. M. Batzill and U. Diebold, *Prog. Surf. Sci.*, **79**, 47 (2005).
31. M. V. Reddy, G. V. Subba Rao, and B. V. R. Chowdari, *Chem. Rev.*, **113**, 5364 (2013).
32. A. Nie, L.-Y. Gan, Y. Cheng, H. Asayesh-Ardakani, Q. Li, C. Dong, R. Tao, F. Mashayek, H.-T. Wang, U. Schwingenschlögl, R. F. Klie, and R. S. Yassar, *ACS Nano*, **7**, 6203 (2013).
33. J. Zhu, Z. Lu, S. Aruna, D. Aurbach, and A. Gedanken, *Chem. Mater.* **12**, 2557 (2000).
34. F. Li, D.-M. Tang, Y. Chen, D. Golberg, T. Kitaura, T. Zhang, A. Yamada, and H. Zhou, *Nano Lett.*, **13**, 4702 (2013).
35. F. Li, D.-M. Tang, Z. Jian, D. Liu, D. Golberg, A. Yamada, and H. Zhou, *Adv. Mater.*, **26**, 4659 (2014).
36. K. U. Schwenke, M. Metzger, T. Restle, M. Piana, and H. A. Gasteiger, *J. Electrochem. Soc.*, **162**, A573 (2015).
37. N. B. Aetukuri, B. D. McCloskey, J. M. García, L. E. Krupp, V. Viswanathan, and A. C. Luntz, *Nature Chemistry*, **7**, 50 (2015).
38. S. Meini, M. Piana, N. Tsiouvaras, A. Garsuch, and H. A. Gasteiger, *Electrochem. Solid State Lett.*, **15**, A45 (2012).
39. J. Zhang and L. Gao, *Mater. Chem. Phys.*, **87**, 10 (2004).
40. M. Pourbaix, *Atlas of Electrochemical Equilibria in Aqueous Solutions*, 2nd English ed., chapter IV, section 17.4, p.478, Fig. 1, and chapter IV, section 18.4, p.527, Fig. 1, National Association of Corrosion Engineers, Houston (1974).
41. M. Piana, J. Wandt, S. Meini, I. Buchberger, N. Tsiouvaras, and H. A. Gasteiger, *J. Electrochem. Soc.*, **161**, A1992 (2014).
42. N. Tsiouvaras, S. Meini, I. Buchberger, and H. A. Gasteiger, *J. Electrochem. Soc.*, **160**, A471 (2013).
43. J. Rockenberger, U. zum Felde, M. Tischer, L. Tröger, M. Haase, and H. Weller, *J. Chem. Phys.*, **112**, 4296 (2000).
44. V. Müller, M. Rasp, J. Rathousky, B. Schütz, M. Niederberger, and D. Fattakhova-Rohlfing, *Small*, **6**, 633 (2010).
45. B. D. McCloskey, A. Valery, A. C. Luntz, S. R. Gowda, G. M. Wallraff, J. M. Garcia, T. Mori, and L. E. Krupp, *J. Phys. Chem. Lett.*, **4**, 2989 (2013).
46. M. Metzger, C. Marino, J. Sicklinger, D. Haering, and H. A. Gasteiger, *J. Electrochem. Soc.*, **162**, A1123 (2015).
47. M. Metzger, B. Strehle, S. Solchenbach, and H. A. Gasteiger, *J. Electrochem. Soc.*, **163**, A798 (2016).
48. V. Viswanathan, K. S. Thygesen, J. S. Hummelshoj, J. K. Norskov, G. Girishkumar, B. D. McCloskey, and A. C. Luntz, *J. Chem. Phys.*, **135**, 214704 (2011).
49. International Centre for Diffraction Data, JCPDS-ICDD Card No: 01-075-2894.